TU Delft

Delft University of Technology

Tantalum-palladium alloy based optical micro-mirror hydrogen sensor

Verhoeff, D. J.; Schreuders, H.; Bannenberg, L. J.

DOI
10.1016/j.snb.2025.137229

Publication date
2025

Document Version
Final published version

Published in
Sensors and Actuators B: Chemical

Citation (APA)
Verhoeff, D. J., Schreuders, H., & Bannenberg, L. J. (2025). Tantalum-palladium alloy based optical micro-mirror hydrogen sensor. *Sensors and Actuators B: Chemical*, *428*, Article 137229. https://doi.org/10.1016/j.snb.2025.137229

Important note
To cite this publication, please use the final published version (if applicable).
Please check the document version above.

Copyright
Other than for strictly personal use, it is not permitted to download, forward or distribute the text or part of it, without the consent of the author(s) and/or copyright holder(s), unless the work is under an open content license such as Creative Commons.

Takedown policy
Please contact us and provide details if you believe this document breaches copyrights.
We will remove access to the work immediately and investigate your claim.

This work is downloaded from Delft University of Technology.
For technical reasons the number of authors shown on this cover page is limited to a maximum of 10.

Sensors & Actuators: B. Chemical 428 (2025) 137229

Contents lists available at ScienceDirect

Sensors and Actuators: B. Chemical

journal homepage: www.elsevier.com/locate/snb

Tantalum-palladium alloy based optical micro-mirror hydrogen sensor

D.J. Verhoeff, H. Schreuders, L.J. Bannenberg *

Faculty of Applied Sciences, Delft University of Technology, Mekelweg 15, 2629 JB Delft, The Netherlands

ARTICLE INFO

Keywords:
Optical hydrogen sensing
Metal hydrides
Thin films
Micro-mirror

ABSTRACT

Optical hydrogen sensors based on metal hydrides have distinct advantages over other types of hydrogen sensors as they can be made small, do not require the presence of oxygen, and have a large sensing range. The working principle is based on the fact that when exposed to an atmosphere containing hydrogen, a metal hydride absorbs hydrogen, which in turn changes the optical properties. In a micro-mirror configuration, this change in optical properties can be measured by measuring the reflectivity of light. Tantalum alloys have been identified as suitable sensing material owing to their large sensing range, hysteresis-free response and fast response times. Here, we rationally develop a micro-mirror hydrogen sensor based on a tantalum-alloy as sensing layer. We first study the optical contrast of $Ta_{0.88}Pd_{0.12}$ thin films with a $Pd_{0.6}Au_{0.4}$ catalyst layer deposited on substrates with various catalyst and sensing layer thicknesses in reflection. Modeling the experimental results shows that the total optical contrast, that is the change of the reflectivity with a changing hydrogen concentration, is a strong interplay of wavelength and hydrogen-concentration dependent reflection, attenuation and amplification coefficients of both the $Ta_{0.88}Pd_{0.12}$ thin films with a $Pd_{0.6}Au_{0.4}$ catalyst layer. These effects may either constructively or destructively contribute to the overall signal, making carefully choosing the wavelength and layer thicknesses essential. Using optimal values of the wavelength and layer thicknesses, we successfully construct and test a micro-mirror sensor that can detect hydrogen over at least 5 orders of magnitude in hydrogen concentration without any hysteresis.

1. Introduction

Hydrogen sensors are likely to increase in importance as the use of hydrogen as an energy carrier is expected to increase, in light of the transition to a carbon-negative society. At present, hydrogen sensors are predominantly used for safety applications, i.e. to detect leaks, as mixtures of hydrogen and air are flammable or even explosive when the hydrogen concentration exceeds 4% in air. These sensors mainly rely on catalytic combustion or thermal conductivity sensors [1,2]. Compared to conventional hydrogen sensors, optical hydrogen sensors have the advantages that they feature a large hydrogen sensing range down to the p.p.m. or even the p.p.b. level [3–5] that is completely reversible and free of hysteresis. Apart from that, optical hydrogen sensors do not require the presence of oxygen and are intrinsically safe as no currents near the sensing area are used [1,6–13]. For these reasons, such sensors can, besides leak detection for safety purposes, also be used for performance optimization in hydrogen fuel cells and electrolyzers or discovering the tiniest leaks that may not cause safety problems but are relevant in light of efficiency or to mitigate climate effects as the presence of hydrogen itself indirectly contributes to the greenhouse effect [14–20].

Optical hydrogen sensors rely on a hydrogen sensing material that partly and gradually absorbs hydrogen when the material is exposed to a hydrogen containing environment. In turn, the absorption of hydrogen results in a change of the optical properties of the material. By probing e.g. these changes by measuring the transmission, reflectivity or (localized) surface plasmon resonances, one can thus probe the hydrogen concentration. As a hydrogen sensing material, palladium and its alloys are often used which is attractive as it can generate an optical contrast and catalyze both the dissociation of molecular hydrogen into atomic hydrogen that is necessary for the hydrogen be absorbed by the material [7,9–11,13,21–23]. However, palladium itself features only a modest sensing range with strong hysteresis as well as sluggish response times and poor long term stability. As such, it is often alloyed with elements including Au to reduce/eliminate the hysteresis arising from a first-order phase transition upon hydrogen sorption. Alloying typically also improves the response time, stability and limit-of-detection of the sensor. However, it also drastically lowers the optical response and thus the sensitivity of the sensor [3,5,24–33].

Differently, one can separate the hydrogen sensing and dissociation functionality and use a tantalum-based hydrogen sensor [4,34–

* Corresponding author.
E-mail address: l.j.bannenberg@tudelft.nl (L.J. Bannenberg).

https://doi.org/10.1016/j.snb.2025.137229
Received 19 September 2024; Received in revised form 16 December 2024; Accepted 2 January 2025
Available online 11 January 2025
0925-4005/© 2025 The Authors. Published by Elsevier B.V. This is an open access article under the CC BY license (http://creativecommons.org/licenses/by/4.0/).

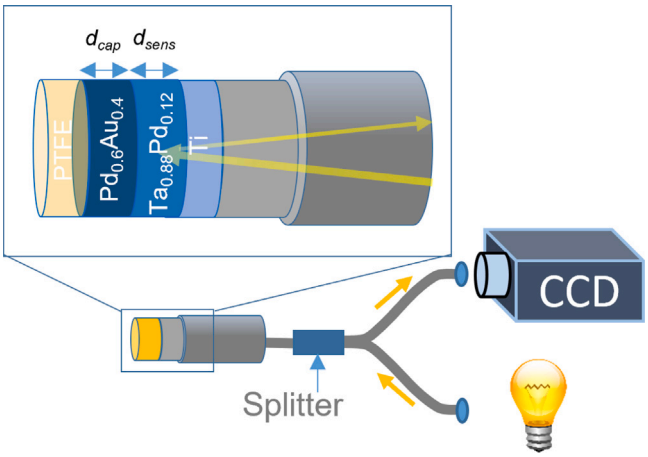

Fig. 1. Schematic representation of a micro-mirror sensor. In such a sensor, light is coupled into the fiber and reflected by the sensing stack on tip of the fiber. The reflected light is subsequently detected by a detector such as a CCD or photodiode. The sensing stack consists out of a Ti adhesion layer, a d_{sens} thick $Ta_{0.88}Pd_{0.12}$ sensing layer, a d_{cap} thick $Pd_{0.6}Au_{0.4}$ capping layer to promote the dissociation of molecular into atomic hydrogen and provide protection against oxidation and a PTFE polymeric protective layer. When hydrogen is present in the proximity of the fiber tip, the sensing layer absorbs hydrogen, changing its optical properties, and thus changing the intensity of the detected reflected light.

38]. In such a sensor, a tantalum-alloy generates the optical contrast while a suitable capping layer, often a palladium alloy, is used to promote hydrogen dissociation [39]. Such a sensor features an enormous sensing range of over 7 orders of magnitude in hydrogen pressure/concentration that is completely reversible and free of any hysteresis. However, while multiple tantalum-alloys have been considered so far, all these studies where based on optical transmission measurements. For a fiber-based sensor, which are advantageous due their small size, possibility to separate readout and sensing area, and ease of integration, one has several options such as a fiber-Bragg grating, surface-plasmon resonance sensor or a micro-mirror sensor. Of these configurations, the micro-mirror sensor is the most simple one. In this configuration, the sensing stack is applied on the tip of an optical fiber [11,13,22,40]. As illustrated in Fig. 1 light, which is coupled into the fiber is partly reflected by this sensing stack. Subsequently, the light passes back through the fiber and a beam splitter and its intensity is detected. Upon exposure to hydrogen, the reflectivity of the sensing stack changes and as a result a different intensity is detected.

The purpose of this paper is to realize a micro-mirror optical hydrogen sensor with a tantalum-palladium alloy as active hydrogen sensing material. In this sensor, we use at least three layers: (i) a 4 nm Ti layer to promote adhesion and the growth of the α-$Ta_{0.88}Pd_{0.12}$ phase, (ii) a $Ta_{0.88}Pd_{0.12}$ sensing layer to generate an optical contrast. From all Ta-alloys, a $Ta_{0.88}Pd_{0.12}$ with thickness d_{sens} is selected as optical transmission measurements indicate that it is a material that has large sensing range of 7 orders of magnitude in partial hydrogen pressure/concentration, while fewer hydrogen molecules need to be dissociated and transported than for e.g. Ta. (iii) We use a d_{cap} thick $Pd_{0.6}Au_{0.4}$ as capping layer to prevent oxidation and promote the hydrogen dissociation. $Pd_{0.6}Au_{0.4}$ is selected as previous research shows that it does not generate a hysteric optical response to hydrogen such as for more palladium-rich Pd-alloys [39]. A polymeric layer is used as a fourth optional layer to protect the capping layer from poisoning by chemical species such as CO, H_2S and NO_x as well as further promoting the hydrogenation kinetics [3,41,42].

The structure of this paper is as follows. First, we describe the contributions of the various layers to the signal. Second, we perform measurements on quartz substrates in reflection to obtain information on wavelength, capping- and sensing layer thickness dependence of the optical contrast upon exposure of various stack configurations. Third, we use the reflectivity measurements on the different sample stacks to model the optical response. Finally, we present measurements of micro-mirror hydrogen sensor realized by depositions on the tip of an optical fiber.

2. Experimental

2.1. Sample fabrication

All layers are created by magnetron sputtering, a technique that allows the coating of a substrate or fiber with a material by the deposition of atoms of a target material at a constant rate. Depositions have been performed both on fused quartz substrates and the tip of optical fibers. As substrates, we used 10 × 10 × 0.5 mm^2 in size, with a surface roughness < 0.4 nm (Mateck GmbH, Jülich, Germany). For the fibers, multimode glass fibers with a diameter of 200 μm and a numerical aperture of 0.48 (Thorlabs, Inc., Newton, New Jersey, United States of America) have been used. To perform deposition on the tip of an optical fiber, a special sample holder was used. Before the deposition, the fiber coating is removed with a fiber stripping tool (Thorlabs, Inc., Newton, New Jersey, United States of America) after which the fiber is thoroughly cleaned with isopropanol to remove any residual coating material. The fibers are cleaved with a diamond-tipped cleaving instrument (Vytran, LDC-200) perpendicular to the length of the fiber to achieve a flat deposition surface.

The metallic adhesion, sensing and catalyst layers of our samples are synthesized with direct current magnetron sputtering. This sputter process is performed in 0.3 Pa of Argon and inside an AJA Int. ultrahigh vacuum chamber with a base pressure of 10^{-6} Pa. The metallic targets (5.08 mm (2 inch) and a purity of at least 99.9%, Mateck GmbH, Jülich, Germany) are all pre-sputtered for approximately 5 min with the exception of Ta, which is pre-sputtered for 60 min to eliminate any possible contamination of nitrides and oxide layers on the surface of the target material. Different from the other layers, an optional PTFE layer is deposited on top of the metallic layers with radio-frequency magnetron sputtering in 0.5 Pa of Ar. Additionally, the substrates are rotated during the exposure to enhance the homogeneity of the deposited layers. The deposition rates of the metallic materials 0.05 nm s^{-1} (100 W DC) for Ti. Unless stated differently, the thickness of this Ti layer that promotes the growth of the body centered cubic α-Ta phase is 4 nm [43]. The $Ta_{0.88}Pd_{0.12}$ layer is prepared by co-deposition of Ta and Pd at 151 and 7 W DC, respectively, with a typical deposition rate of 0.24 nm s^{-1}. Similarly, the $Pd_{0.6}Au_{0.4}$ layer was deposited by co-deposition of Pd and Au at 34 and 19 W DC, respectively, with a typical deposition rate of 0.21 nm s^{-1}. The desired layer thickness of the materials is obtained by a certain exposure time of the substrate to the plasma environment. The sputter rates are determined with tooling samples by sputtering each material independently over a specific time interval at fixed power, after which the thickness of the tooling samples is approximated with X-ray reflectometry measurements. Division of the layer thickness and sputter time will compute the sputter rate per material as result. We note that for practical reasons we used a $Pd_{0.60}Au_{0.35}Cu_{0.05}$ catalyst layer for samples with a 80 nm sensing layer. This we deposited using a custom-made $Pd_{0.60}Au_{0.35}Cu_{0.05}$ target at 50 W DC corresponding to 0.20 nm s^{-1}. We expect no significant variation in the optical contrast because of this difference in the catalyst layer with Cu doping as the hydrogen solubility of the Cu doped capping layer is roughly the same as $Pd_{0.6}Au_{0.4}$ [4] and the optical constants should be roughly the same according to Shiraishi et al. [44].

Before the optical measurements, the samples are subjected to three cycles of 100% hydrogen with a minimum pressure of $P_{H2} = 10^5$ Pa at T = 19.5 °C. This process is not uncommon for metal hydrides. In general, a few cycles of initial exposure to hydrogen is necessary for the thin film micro-structure to settle. The initial rearrangement of atoms could also cause hysteresis in the first few cycles. Reproducible results

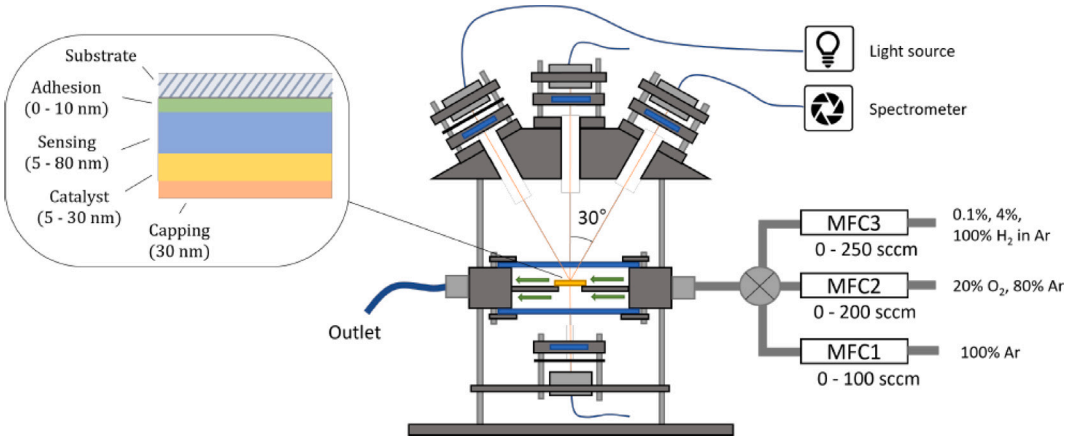

Fig. 2. Schematic representation of the Flow-Setup and sensing stack configuration. The gas chamber is connected to three flow controllers. The desired concentration in the chamber can be achieved by setting the flow of different hydrogen and Ar gas mixtures. The sample is probed with light that is focused on the sample by a lens, after which it is coupled into another optical fiber connected to a spectrometer. Reflection measurements are performed at 30° whereas transmission utilizes a perpendicular beam to the sample.

of the hydrogenation kinetics and optical contrast is achieved after the second cycle of hydrogen exposure. To fully unload the samples, they are subjected for at least two days to a 20% oxygen-rich environment and pressure exceeding 1 bar to extract all hydrogen atoms from the layer.

2.2. Structural measurements

To characterize the crystal structure and thickness of the layers constituting the sensing stack, we use X-ray diffraction and reflectometry measurements on the as-prepared samples. All X-ray measurements are done with a Bruker D8 Discover diffractometer equipped with a Cu tube ($\lambda = 0.1542$ nm) operating at 40 kV, 40 mA and a LYNXEYE XE detector operated in 0D high count rate mode.

To identify the phases and potential contamination of the deposited samples on the substrates we use the Bragg–Brentano geometry for XRD measurements. Samples are placed on a zero diffraction wafer to minimize background scattering. Measurements were performed with a Göbel mirror and a 0.6 mm exit slit on the primary side and two 0.6 mm slits on the secondary side. Exemplary XRD data is displayed in Fig. S3.

To obtain the as-prepared thicknesses of the various layers, we performed X-ray reflectometry measurements. They were performed with a Göbel mirror and a 0.1 mm slit on the primary side and two 0.1 mm slits on the secondary side. The data is subsequently fitted in GenX 3 [45,46], to obtain estimates of the layer thickness, surface roughness and density of the layers. Exemplary XRR data is displayed in Fig. S2.

2.3. Optical measurements

A flow setup was designed for the optical response measurements at room temperature ($T = 19.5 \pm 0.5$ °C) and atmospheric pressure. A schematic representation of the setup is given in Fig. 2. The setup allows for both reflective and transmission measurements such that the different optical responses can be compared. The flow chamber is connected to three flow controllers with a flow of 0–100 s.c.c.m., 0–200 s.c.c.m. and 0–250 s.c.c.m. (Thermal Mass GF Series, Brooks Instrument, Hatfield, PA, United States of America) that determine the flow of the connected gas. To archive different hydrogen concentrations inside the chamber, we use gas mixtures of 0.1% H_2 and 4% H_2 in Argon ($\Delta c_{H2}/c_{H2} < 2\%$, Linde Gas Benelux BV, Dieren, the Netherlands) and 100% H_2 gas combined with 100% Ar gas from the gas network (5N purity). The flow of individual controllers can be adjusted with a National Instruments LABVIEW code to achieve the desired hydrogen concentration in the chamber. This setup allows for a minimum hydrogen concentration of 0.0004% H_2 Hydrogen in Ar, up to 100% H_2. As all the measurements are performed at atmospheric pressure this corresponds to a partial hydrogen pressure range of 0.4 - 10^5 Pa. During measurements, a continuous flow is kept at 100–250 s.c.c.m.. We note that the sensor also works in vacuum and (synthetic) air-hydrogen mixtures.

Light is generated by an Ocean Optics HL-2000-FSHA halogen light source (Ocean Insights, Orlando, FL, United States of America), this creates a spectrum ranging from 300–1200 nm that can be found in Fig. S1. The light source is connected to optical fibers with diameters ranging from 50 to 600 μm. Intensity of the light from the fiber can be adjusted with a Thorlabs Cage System Iris Diaphragm with a diameter of 0.8–20 mm (Thorlabs, Inc, Newton, New Jersey, United States of America), after which it is focused on the sample with lenses. The reflected or transmitted light is coupled into another optical fiber connected to an Ocean Insight Maya2000 Pro Series Spectrometer (Ocean Insights, Orlando, FL, United States of America). The frequency for which the spectra are sampled ranges from 1 Hz to 0.1 Hz. During processing of the data, we corrected the output from the spectrometer by subtracting the background signal of the spectrometer obtained from a measurement with the shutter closed (‘dark’ measurement).

For the reflective measurements, the light source and spectrometer are positioned at a 30° angle such that measurements are minimally dependent on the angle of the incoming light with the size of the setup in mind. The optomechanical components used in the setup are provided by Thorlabs (Thorlabs, Inc, Newton, New Jersey, United States of America). For the absolute optical reflectivity an Ocean Optics PTFE fiber optic integrating sphere with a Lambertian surface was used (>98% reflectivity).

We designed the flow chamber with fiber adapters such that we can measure the performance of the optical fiber samples in the same set-up. Fibers are secured with an epoxy resin (Torr Seal epoxy resin) in the fiber connectors to ensure a leak-tight connection. A beam splitter with a core diameter 200 μm (Ocean Optics QBif200-vis-BX) is connected to the light source, and the reflected signal is measured by the spectrometer as depicted in Fig. 3.

The absolute optical transmission has been measured using an Ocean Optics DH-2000BAL deuterium-halogen light source, and an HR4000 Ocean Optics Si-based array spectrometer in a fiber optic setup.

2.4. Model

The experimental data is modeled using the model described in Sections 3.1 and 3.3 with a home written Python code. The model is

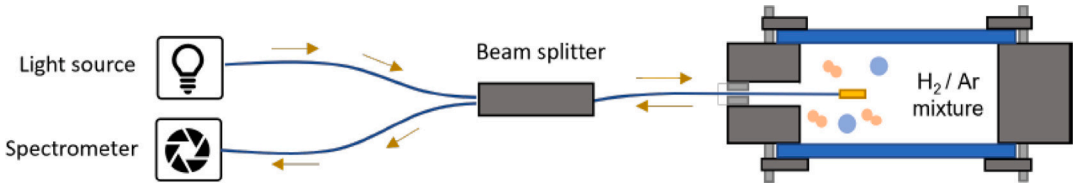

Fig. 3. Schematic representation of the flow-setup with fiber adapter. The sensing layer on the tip surface is probed with the same light source as in Fig. 2 after traveling through the beam splitter device and reaching the spectrometer.

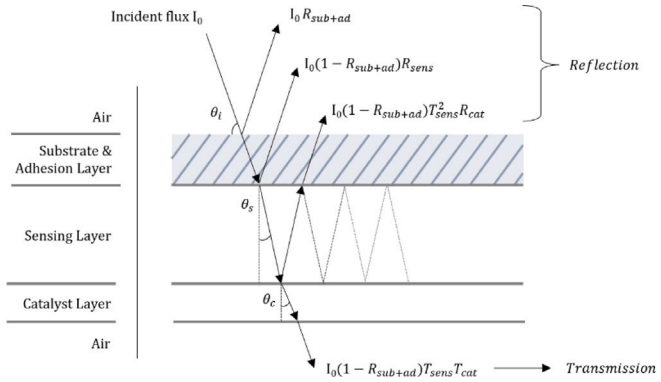

Fig. 4. Schematic representation of the light propagation and corresponding reflection and transmission signal of the hydrogen sensing system at the various layers.

fit to the data to obtain estimates of the attenuation, amplification and reflection coefficients as a function of wavelength and partial hydrogen pressure. To do this, we define a loss function that returns the squared difference between the modeled value and the experimental of all the individual data points with different sensing and cap layer thickness to the experimental data (either the optical transmission or reflection) to the theoretical model as follows:

$$\min_{R_{sub},R^*_{sens},R^*_{cap},\kappa_{sens},\kappa_{cap},\alpha_{sens}} \left\{ \sum_{d_{sens}} \sum_{d_{cap}} \left[Model(\lambda, P_{H2}, d_{sens}, d_{cap}) - Exp.(\lambda, P_{H2}, d_{sens}, d_{cap}) \right]^2 \right\} \quad (1)$$

The minimization problem requires an initial guess, where we provide the theoretical reflections of the materials without hydrogen according to Fresnel's law and initial guesses for other parameters according to experimental findings. To ensure robust results, we iterate the loss function over a large extend of other possible combinations of initial guesses for unknown parameters and set bounds for the theoretical minimum and maximum values parameters.

3. Results

3.1. Sensing stack geometry

Before we present the results of the optical measurements, we refer to Fig. 4 for a description of the reflected signal in the system. Neglecting secondary reflections, the total signal of our samples is mainly governed by three reflections: (i) the initial reflection on the substrate and adhesion later, (ii) the reflection from the sensing layer and (iii) reflection from the catalyst layer. In the absence of fluorescence and interference ($d \ll \lambda$), the incident light flux propagating upon and through an absorbing material i is described by the reflection, absorption and transmission. We find that we can approximate the light intensity in a layer of our extremely thin metal-hydride film system by a series of mathematical expressions. We refer to a later section for the derivation of these expressions.

- Reflection (R^*_i, κ_i, z): The intensity of the reflection upon an absorbing media can be described by its intrinsic reflectance $R^*_i(n_i, \kappa_i, \theta)$ which can be determined by Fresnel's equations. However, it turns out that in a extremely thin film system, the reflection intensity is also determined by the path length (z) of the light, which is directly related to the thickness of the material. Based on experimental findings and a previous study [47], to describe this phenomenologically, we propose that this thickness dependence follows an exponential increasing function ($1 - \exp^{-\kappa_i z}$), where κ_i is an amplification coefficient that governs the shape of the function.
- Absorption (α_i, z): Absorption in an absorbing medium is described by the absorptivity, in this case governed by the absorption coefficient $\alpha(k, \lambda)$ and the path length traveled.
- Transmittance: The portion of light that is not reflected or absorbed is transmitted and is described by $T = \frac{I(z)}{I_0}$ where I is the intensity of the light. The transmittance can be approximated by Lambert's law $T = (1 - R)e^{-\alpha z}$ where we account for reflection losses by subtracting it from the incident flux.

An incident light flux is first reflected by the substrate and adhesion layer. When it reaches the sensing layer, it can either be absorbed (α_{sens}) or reflected (R^*_{sens}, κ_{sens}), where the reflected light from the sensing layer contributes the total reflected intensity. When it has passed through the sensing layer, a portion of the light will be reflected from the catalyst layer (R^*_{cat}, κ_{sens}). After which it has to pass through the sensing layer again to contribute to the total reflected intensity and is thus attenuated twice in the sensing layer. The final portion of the transmitted light will reach the catalyst-air interface, where we can calculate the reflection according to the Fresnel equations without the complex refraction coefficient, as air is a non-absorbing medium. Based on data from Ref. [30], we compute that for $Pd_{0.6}Au_{0.4}$ in contact with air, the reflected intensity will be well below 0.1% for light in the visible wavelength range. Therefore, we thus assume total transmission through the catalyst - air interface. As a result, the intensity of the reflected light depends on the following parameters; R^*_{sens}, R^*_{cat}, κ_{sens}, κ_{cat} and α_{sens}. This raises the question which of the parameters changes upon absorption of hydrogen in the sensing layer and, in turn, in what magnitude the evolution of these parameters influences the optical contrast $\frac{R}{R_0}$. To approximate the change in the individual parameters upon hydrogen absorption, a model is created to which we fit the experimental data. Results thereof are presented in Section 3.3.

3.2. Substrate measurements

First we will discuss the change of the reflectivity obtained for various sensing stack configurations by variation of the sensing- and catalyst layer thicknesses (d_{sens}, d_{cat}) and the dependence on the wavelength λ. To this end, Figs. 5(a)–(c) and (d)–(f) depict the relative change of the reflectivity as a function of wavelength when a hydrogen concentration step is performed from C_{H2} = 0% to 0.016% and C_{H2} = 0.016% to 4%, respectively. In the figure, we display the optical contrast for various thicknesses of the sensing and catalyst layer. These two hydrogen concentrations steps are chosen as the first step shows the optical contrast at very low hydrogen concentration that are particularly relevant for determining small hydrogen leaks, while the second

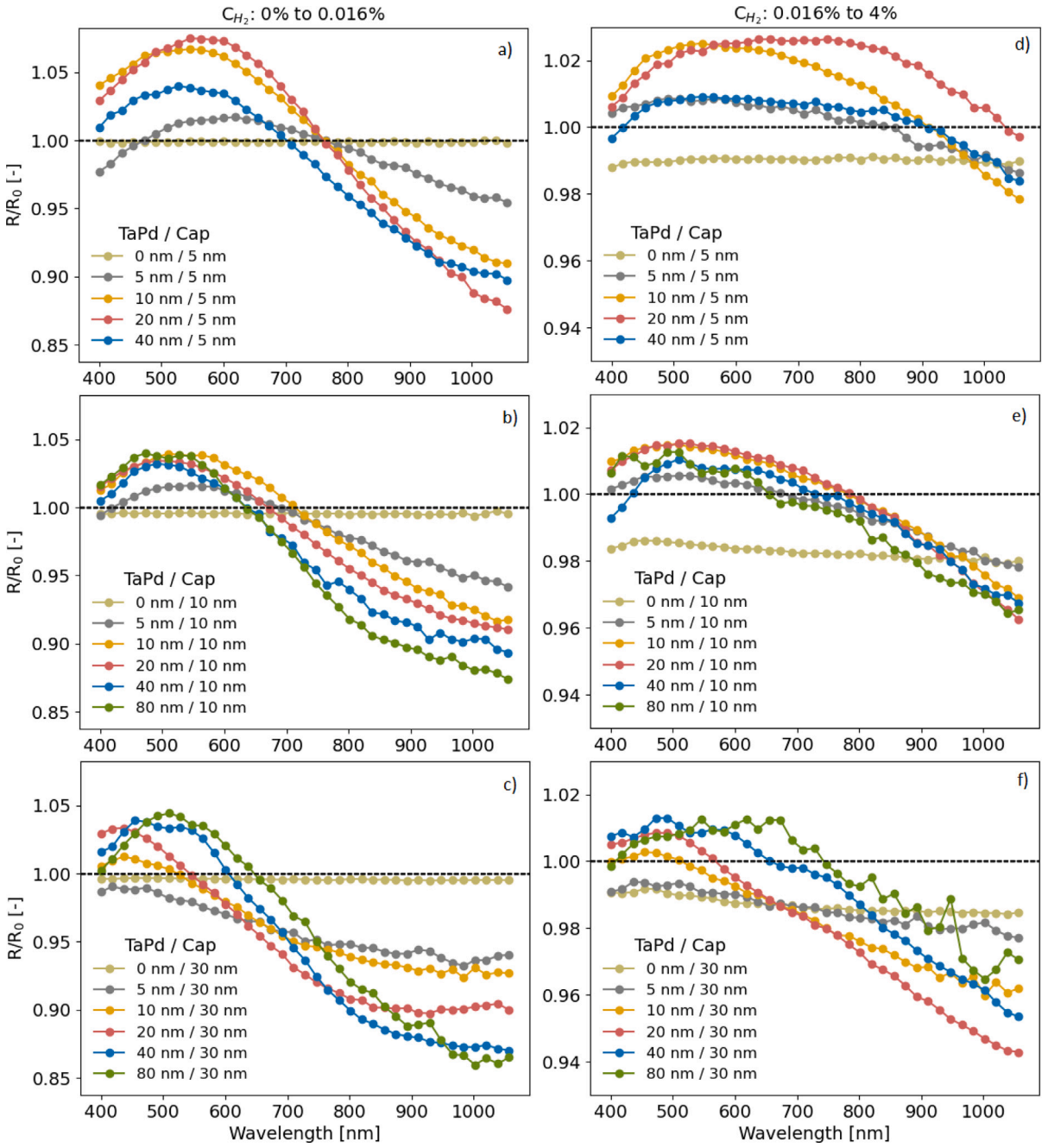

Fig. 5. Spectroscopic optical response of 12 different samples with various sensing stack dimensions upon a hydrogen concentration step of (a)–(c) C_{H2} = 0% to 0.016% and (d)–(f) C_{H2} = 0.016% to 4%, the color of the data represents distinct sensing layer thicknesses. The sensing layer consists of $Ta_{0.88}Pd_{0.12}$, the catalyst layer is $Pd_{0.60}Au_{0.40}$ with a 30 nm PTFE polymer coating, with the exception of the samples with 80 nm sensing layer, which have a $Pd_{0.60}Au_{0}.35Cu_{0.05}$ catalyst layer and no polymer coating.

one is up to the limit of the explosive range of hydrogen of 4% in air. The absolute reflectivity and transmission of selected hydrogen sensing stacks can be found in Figure S4.

We can deduce four general trends in Fig. 5. First, we find that the reflectivity for all sensing stack configurations with $d_{sens} > 0$ display a non-monotonous behavior of the reflectivity with wavelength. For blue (450–500 nm) and green light (500–560 nm), the reflectivity increases when the hydrogen concentration is increased, whereas a profound decrease is observed for infrared light ($\lambda \geq 750$ nm). It indicates that the optical parameters are strong functions of the wavelength. This is strikingly different from when only a $Pd_{0.6}Au_{0.4}$ layer is used (i.e. $d_{sens} = 0$) for which almost no wavelength dependence is observed. It highlights the complex response of $Ta_{0.88}Pd_{0.12}$, which can be beneficial when using multiple wavelengths to produce a hydrogen sensors.

Second, the wavelength-dependence of the change in reflectivity indicates that there are two wavelength regimes particularly attractive when using $Ta_{0.88}Pd_{0.12}$ as a sensing layer for an optical hydrogen sensor in reflection. Indeed, the optical contrast, defined as the magnitude of the relative change of the reflectivity upon exposure to hydrogen, is relatively large around λ = 500 nm (green light) and for λ > 800 nm, i.e. infrared light. Although infrared light seems to provide the largest amount of contrast, we will not disregard the optical contrast in the visible light range. Choosing the wavelength around λ = 500 nm may be better suited when designing a hydrogen sensing system, as components may be cheaper and better suited for visible light compared to infrared or as measuring multiple wavelengths could be beneficial for sensing applications [48].

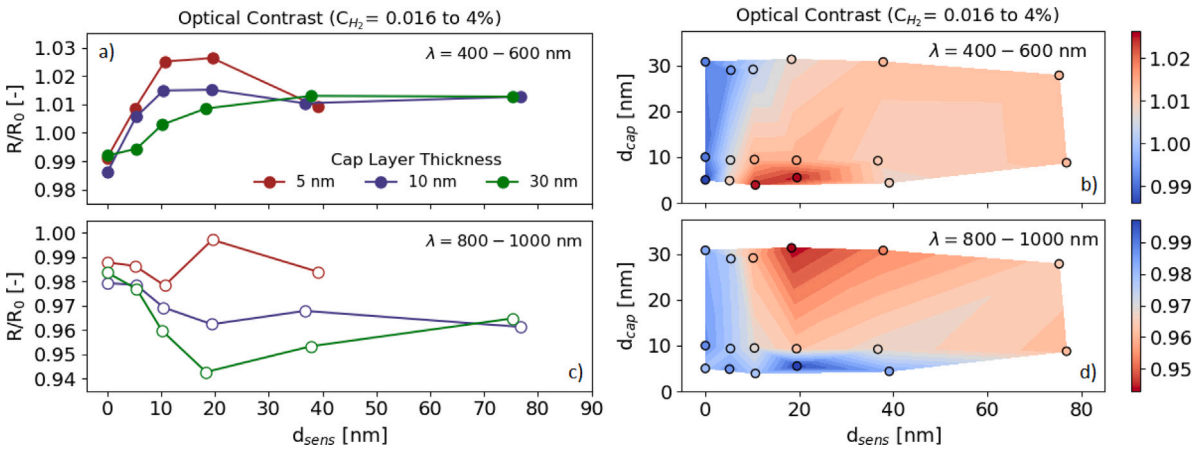

Fig. 6. Maximum optical contrast as a function of sensing layer thickness for samples with different capping layer thicknesses for two wavelength ranges subject to a hydrogen concentration step of 0% to 0.016% for (a) λ = 400–600 nm and (c) λ = 800–1000 nm. (b) & (d) display contour plots of the optical contrast where red indicates highest amount of optical contrast. The thicknesses referred to are the thicknesses determined by XRR measurements.

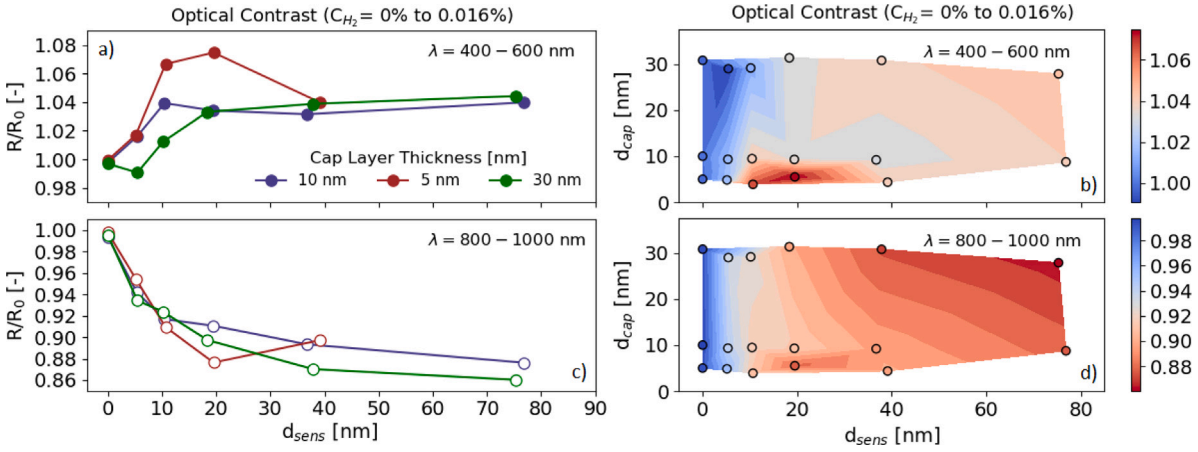

Fig. 7. Maximum optical contrast as a function of sensing layer thickness for samples with different capping layer thicknesses at two wavelength regimes subject to a hydrogen concentration step of 0.016% to 4% for (a) λ = 400–600 nm and (c) λ = 800–1000 nm. (b) & (d) display contour plots of the optical contrast where red indicates highest amount of optical contrast. The thicknesses referred to are the thicknesses determined by XRR measurements.

Third, we find that the samples without a sensing layer do not provide any contrast in the low hydrogen concentration regime. In comparison, it does provide contrast in the high-concentration regime. The root cause of this is that the hydrogen solubility at low hydrogen concentrations of the catalyst layer is significantly smaller than that of the sensing layer and only begins to absorb a noteworthy amount of hydrogen around $P_{H2} \approx 1000$ Pa ($C_{H2} \approx 1\%$) [27,29,38]. Correspondingly, for the step from C_{H2} = 0.016% to 4%, we observe a decrease in the reflection intensity of the catalyst layer and the material becomes more transparent.

Most important of all, the layer dimensions have a considerable influence on the optical contrast of our system. Especially the catalyst layer thickness has a profound impact on the optical contrast for small sensing layer thicknesses as illustrated in Fig. S5. This is even the case for the step of C_{H2} = 0% to 0.016% where the catalyst layer itself does not absorb any hydrogen.

3.2.1. Sensing stack thickness

Following the pronounced influence of the layer thicknesses on the optical contrast, we want to select a combination of the sensing layer and catalyst layer thickness that provides that largest contrast. In addition to the optical considerations, we have the following design considerations with regard to the layer thicknesses: (i) the capping layer thickness should be $d_{cap} \gtrsim 5$ nm to ensure a coherent layer that fully covers the surface of the $Ta_{0.88}Pd_{0.12}$ sensing layer and (ii) the sensing layers should be as thin as possible such that the least amount of hydrogen needs to be dissociated and transported. Especially the absolute amount of hydrogen that needs to be dissociated is important, as this is determined to be the rate-limiting step [39] (see, e.g., Ref. [4] for response time measurements on the same material stack). (iii) When possible, a thinner capping layer is preferred as it saves material costs and deposition time while also the diffusion length is shorter (although this is not rate limiting).

To study the layer thickness dependence of the optical contrast in reflection, Figs. 6 and 7 display the maximum optical contrast of all sensing stack configurations for both visible light (λ = 400–600 nm) and infrared light (λ = 800–1000 nm) for a hydrogen concentration step of 0% to 0.016% and 0.016% to 4%, respectively. The choice to study both wavelength regimes separately is based on Fig. 5 where we found that both regimes provide opposite and substantial optical responses to hydrogen. Both regimes can thus be beneficial to construct a hydrogen sensor.

Figs. 6(a) and 7(a) show that the catalyst layer significantly influences the optical contrast in the visible light regime. Most remarkable, the samples with a 10 and 20 nm sensing layer combined with a 5 nm catalyst layer provide more optical contrast than the thicker 40 nm sample in both regimes. The larger response of the 10 and 20 nm sensing layers compared to the 40 nm sensing layer is at first glance non-intuitive. We would expect a more prominent contrast of thicker sensing layers, just as with samples measured in transmission. As we

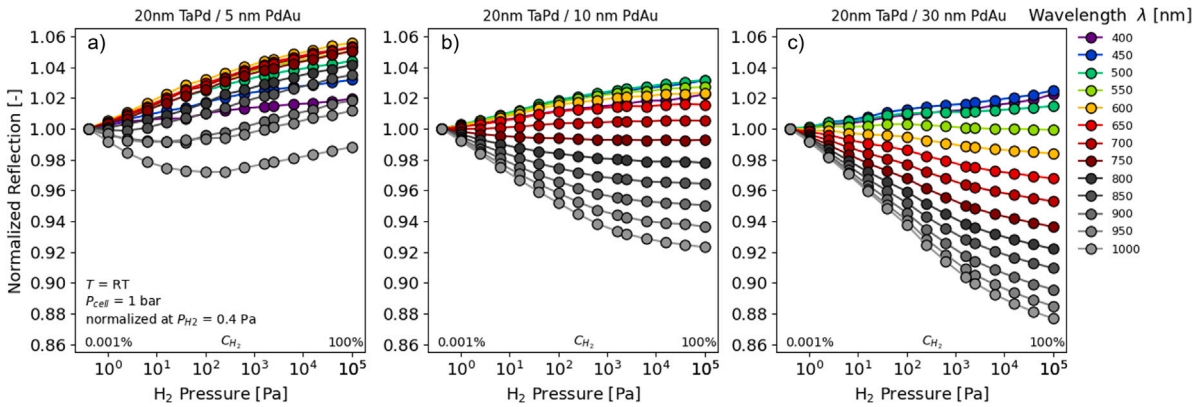

Fig. 8. Optical reflectivity as a function of the partial hydrogen pressure normalized to the reflectivity at P_{H2} = 0.4 Pa. ('PRI diagrams') of 3 different samples with a 3 nm Ti, 20 nm $Ta_{0.88}Pd_{0.12}$ sensing layers and a (a) 5 nm, (b) 10 nm and (c) 30 nm $Pd_{0.6}Au_{0.4}$ capping layer. All samples have a 30 nm PTFE polymer coating and have been measured at 1 bar and room temperature for at partial hydrogen pressures ranging from 0.4 Pa to 10^5 Pa, i.e. corresponding to $0.0004\% \leq C_{H2} \leq 100\%$. The wavelengths are binned in groups of 50 nm.

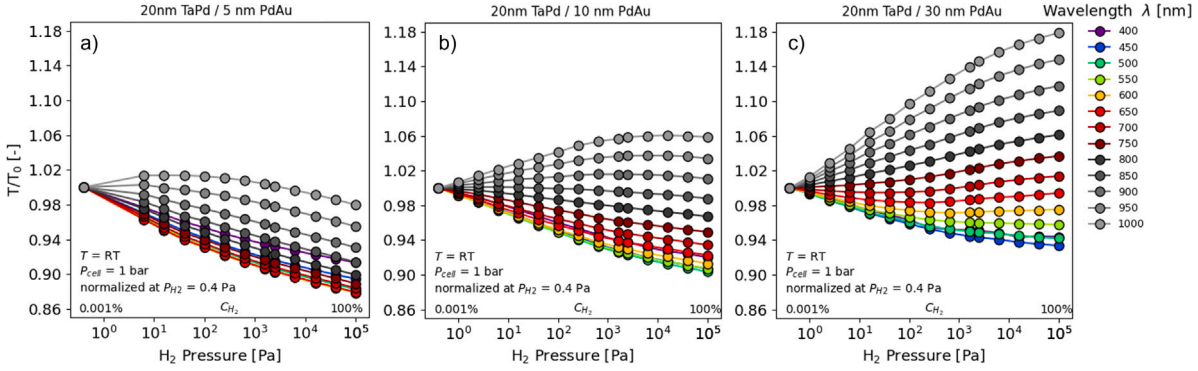

Fig. 9. Optical transmission as a function of the partial hydrogen pressure normalized to the transmission at P_{H2} = 0.4'Pa. ('PTI diagrams') of 3 different samples with a 3 nm Ti, 20 nm $Ta_{0.88}Pd_{0.12}$ sensing layers and a (a) 5 nm, (b) 10 nm and (c) 30 nm $Pd_{0.6}Au_{0.4}$ capping layer. All samples have a 30 nm PTFE polymer coating and have been measured at 1 bar and room temperature for at partial hydrogen pressures ranging from 0.4 Pa to 10^5 Pa, i.e. corresponding to $0.0004\% \leq C_{H2} \leq 100\%$. The wavelengths are binned in groups of 50 nm.

will see later by modeling the response, this phenomenon is attributed to an increase of the κ_{sens} parameter upon hydrogen loading of the sensing layer in the visible light. However, the change in this parameter only significantly affects thin sensing layer dimensions. For a sensing layer with a thickness of 40 nm or larger, the contrast is almost only generated by the change in intrinsic reflectance R^*_{sens}.

Differently, the influence of the change in κ_{sens} upon hydrogen loading is not seen in the samples with 10 nm and 30 nm catalyst layers because the larger reflection from the catalyst layer counters its contribution to the contrast. These results imply that we can tune both the sensing and catalyst layer dimensions to optimize the optical contrast. The contrast values in the visible light of all samples with varying catalyst layers converge at a sensing layer of 40 nm or larger. This phenomenon can be clarified because most transmitted light is already attenuated (either reflected or absorbed) when it reaches the catalyst layer for samples with $d_{sense} \geq 40$ nm. As such, the catalyst does not influence the response.

Furthermore, from Figs. 6 and 7 we observe that the optimal layer thicknesses when using visible light are the same for the two hydrogen concentration steps considered (d_{sens} = 20 nm, d_{cap} = 5 nm). For the infrared regime, multiple options are possible. A configuration with a thick sensing layer $d_{sens} \approx 80$ nm provides a large optical contrast, irrespective of the capping layer thickness. However, such a thick sensing layer would result in relatively long response times. Differently, d_{sens} = 20 nm, d_{cap} = 30 nm also provides a good response, but with a four times thinner sensing layer and thus a response time that is about 4 times shorter.

3.2.2. Full range

To characterize the sensing response across an even wider hydrogen concentration range, the samples are subject to a hydrogen concentration range of $0.0004 \leq C_{H2} \leq 100\%$. At atmospheric pressure, this results in a partial hydrogen pressure range of $0.4 \leq P_{H2} \leq 10^5$ Pa. To get the optical reflectivity changes as a function of the concentrate range, we stepwise increased and decreased the hydrogen concentration. An example of this data, confirming that the response is free of any hysteresis, can be found in Fig. S6. On the basis of this data, we determine the pressure optical-transmission isotherm (PTI) or pressure optical-reflection isotherm (PRI) by taking the optical transmission/reflection in thermodynamic equilibrium at a specific partial hydrogen pressure/concentration. The resulting PRIs/PTIs thus provides the change in optical contrast as a function of partial hydrogen pressure at a particular temperature.

Figs. 8 and 9 provides the PRI/PTI diagrams at different wavelengths for samples with a 20 nm $Ta_{0.88}Pd_{0.12}$ sensing layer and a $Pd_{0.6}Au_{0.4}$ catalyst layer with d_{cap} = 5, 10 and 30 nm. With the PRIs/PTIs we can distinguish if the optical contrast changes monotonically with increasing hydrogen pressure. This is essential for hydrogen sensors; if this is not the case, a sensor readout can correspond to two (or more) different hydrogen pressures and the hydrogen pressure can thus not be uniquely defined.

Starting with the PRIs of the sample with a 5 nm catalyst layer in reflection (Fig. 8), we observe an almost linear monotonic increase of the reflection of the λ = 400–700 nm light with increasing hydrogen pressure across the entire measured pressure range. The highest sensitivity can be obtained by measuring the yellow λ = 600 nm light as it

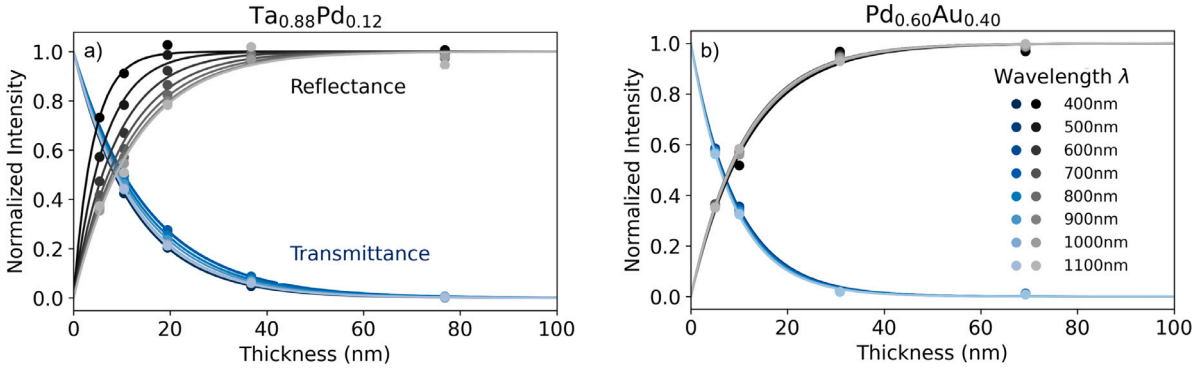

Fig. 10. Normalized reflectance and transmittance intensity of unloaded materials at different thickness for different wavelengths. The reflection data is measured at an 30° angle and the transmission perpendicular to the samples. (a) $Ta_{0.88}Pd_{0.12}$, (b) $Pd_{0.60}Au_{0.40}$, the solid line display a fit to the data.

has the largest monotonic change in reflected intensity with increasing hydrogen pressure.

For infrared light, a non-monotonic relationship between hydrogen pressure and reflected intensity is apparent making the sample with a 5 nm catalyst layer unsuitable for hydrogen sensing. Luckily, this behavior is not seen in the measurements of the 10 nm and 30 nm catalyst layer samples. It implies that the reflection from the catalyst layer is a key parameter that governs the optical response of infrared light. When the reflection from the catalyst layer decreases, it induces a non-monotonic relation of the optical contrast against hydrogen pressure for infrared light. This displays the delicate balance in the changing optical parameters upon hydrogen absorption and their ability to counter each other.

The 30 nm catalyst layer sample displays the largest change in reflected intensity for infrared light in combination with a monotonic decrease in intensity as hydrogen pressure increases across the entire investigated sensing range. Taken together, the largest sensitivity for a 20 nm sensing layer with a non-monotonic increase can be obtained for infrared light with a 30 nm capping layer and for visible light with a 5 nm capping layer.

3.3. Modeling the response

So far, we have seen that the sensing and capping layer thicknesses as well as the wavelength have a profound effect on the direction and magnitude of the optical reflectivity changes. To enhance our understanding, we aim to model these optical changes that can help us to further improve the contrast.

As a first step, we consider the reflection and transmission of an unloaded sensing and catalyst layer deposited on a substrate for various layer thicknesses and wavelengths. These results, displayed in Fig. 10, show for both the reflection and transmission a profound layer thickness dependence. This is expected for the optical transmission, as, according to Lambert's Law, the transmission has an exponential relationship with the thickness d according to $T = \exp^{-\mu d}$. However, it is less trivial for the reflectance. Indeed, in the framework of Fresnel's equations no thickness dependence is incorporated for the reflectance (Fig. S7). Here, however, we also find an exponential relationship according to $R = 1 - \exp^{-\kappa z}$, where κ is an amplification coefficient. We note that similar observations have been made for sputtered Ag films [47]. In addition, we note that for metallic thin films, the reflection may contribute significantly to the loss in transmission of a material.

Following these observations, we modify Fresnel laws with our empirical observations and model the reflection and transmission of light incident on a metal thin film consisting of material i as:

$$R = R_i^*(n_i(x,\lambda), k_i(x,\lambda), \theta)(1 - \exp[-\kappa_i(\lambda,x)z]), \tag{2}$$

$$\begin{aligned} T &= (1-R)\exp[-\alpha_i(\lambda,x)z] \\ &= (1 - R_i^*(n_i(x,\lambda), k_i(x,\lambda), \theta) + R_i^*(n_i(x,\lambda), k_i(x,\lambda), \theta)\exp[-\kappa_i(\lambda,x)z]) \\ &\quad \exp[-\alpha_i(\lambda,x)z] \\ &\approx \exp[-(\alpha_i(\lambda,x) + \kappa_i(\lambda,x))z] \\ &= \exp[-\mu_i(\lambda,x)z], \end{aligned} \tag{3}$$

where we define the attenuation coefficient μ as the combination of the absorption and amplification coefficient $(\alpha(k,\lambda) + \kappa_i)$. This is essentially Lambert's law for materials with high intrinsic reflectivity (R^* close to 1) that also accounts for light attenuation by reflection. The values for κ and μ obtained by fitting the data in Fig. 10 can be found in Table S1.

3.3.1. Modeling the transmission data

Before we analyze the reflection data, we first analyze the transmission data and see if it obeys the relation derived in Eq. (3). The experimental contrast data presented in Fig. 9 reveal that the optical contrast provides two maxima at λ = 500 and 1000 nm. As such, we select these wavelengths for our analysis.

To characterize the optical contrast in transmission upon exposure to hydrogen, we will fit the optical contrast T/T_0 for different sensing layer thicknesses d_{sens} to:

$$\begin{aligned} \frac{T}{T_0} &= \frac{\exp[-\mu(x,\lambda)d_{sens}]}{\exp[-\mu(x=0,\lambda)d_{sens}]} \\ &= \exp[-\Delta\mu(\lambda)d_{sens}]. \end{aligned} \tag{4}$$

where x is the hydrogen-to-metal ratio of the layer (i.e. x in $Ta_{0.88}Pd_{0.12}H_x$) that depends on the hydrogen concentration/partial hydrogen pressure. Fig. 11 presents the results and shows that the model provides a good description of the data and indicates a substantial increase of μ with increasing x/C_{H2} for λ = 500 nm. Differently, μ decreases substantially with increasing x/C_{H2} for λ = 1000 nm.

3.3.2. Modeling the reflection data

Modeling the reflection data is more complicated than modeling the transmission data as multiple reflections (and transmissions) can contribute to the reflected signal from the sensing stack. To model the contrast, we consider the reflection by the substrate/adhesion layer, the reflection of the sensing layer, the transmission of the sensing layer and the reflection of the capping layer. For the optical contrast in reflection, $\frac{R}{R_0}$, this results in the following expression:

$$\frac{R}{R_0} = \frac{R_{sub/ad} + (1-R_{sub/ad})R_{sens,x} + (1-R_{sub/ad})T_{sens,x}^2 R_{cap}}{R_{sub/ad} + (1-R_{sub/ad})R_{sens,0} + (1-R_{sub/ad})T_{sens,0}^2 R_{cap}} \tag{5}$$

where the reflection and transmission in layer with material i are;

$$R = R_i^*(n_i(x,\lambda), k_i(x,\lambda), \theta)(1 - e^{-\kappa_i(\lambda)d_i}) \tag{6}$$

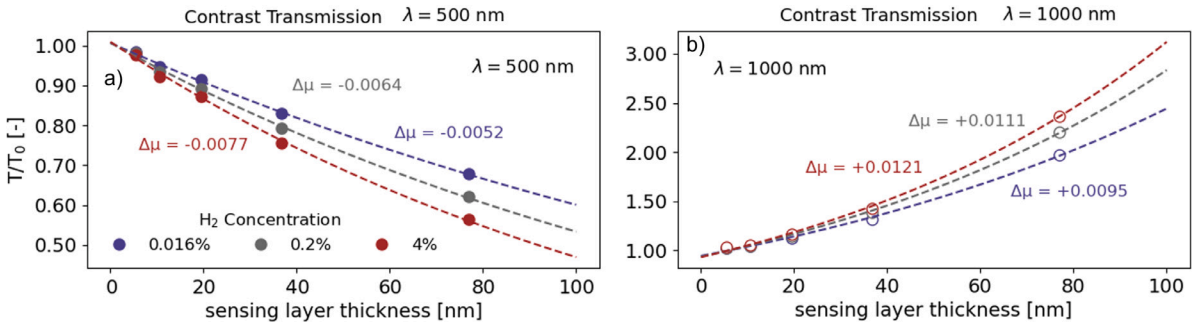

Fig. 11. Fits of the optical contrast in transmission according to Eq. (4) at a hydrogen concentration step of 0% to 0.016%, 0.2% and 4% for (a) λ = 500 nm and (b) fits for the λ = 1000 nm light.

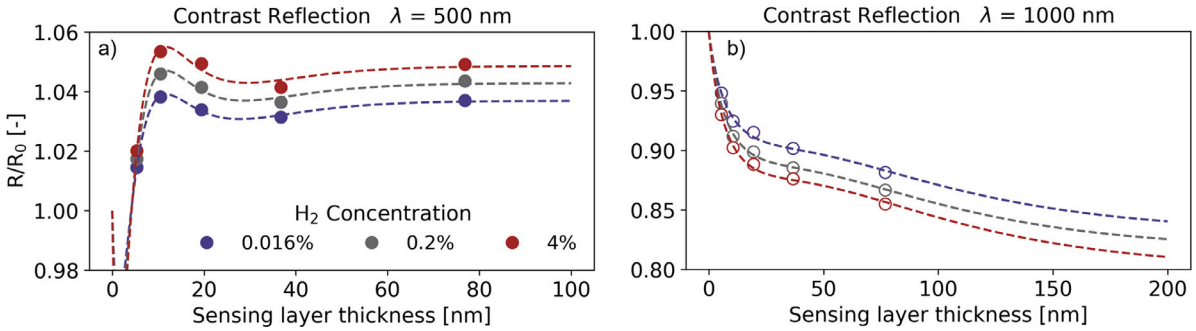

Fig. 12. Fits of the model as presented in Eq. (5) to the experimental optical contrast data in reflection of the 4 nm Ti adhesion layer - d_{sens} $Ta_{0.88}Pd_{0.12}$ sensing layer and 10 nm $Pd_{0.6}Au_{0.4}$ capping layer capped with 30 nm PTFE. The optical contrast is provided upon hydrogen concentration steps from 0 to 0.016%, 0.2% and 4% H_2. The fits are made for both (a) λ = 500 nm light and (b) λ = 1000 nm light with parameters presented in 1.

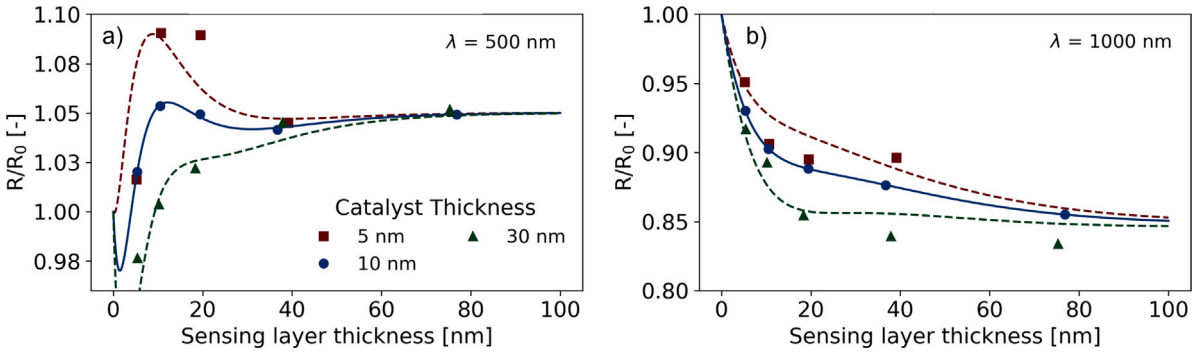

Fig. 13. Optical contrast upon hydrogen concentration from 0 of 4% for (a) λ = 500 nm and (b) λ = 1000 nm of the sensing stacks consisting of a 4 nm Ti adhesion layer, a d_{sens} thick $Ta_{0.88}Pd_{0.12}$ sensing layer and for the $Pd_{0.6}Au_{0.4}$ capping layer thicknesses indicated. The films all have a 30 nm PTFE layer. The continuous lines are the modeled data based on fitting the data of Fig. 12 with parameters presented in 1.

$$T = (1 - R(n_i, k_i, \theta, z))e^{-\alpha_i(k_i,\lambda)d_i} \quad (7)$$

and we assume:

- complete uniformity of the layers and no diffuse scattering,
- no interference influence on the reflected intensity,
- no change in intrinsic reflection of the sensing - catalyst interface upon hydrogen absorption of the sensing layer,
- catalyst layer does not absorb hydrogen,
- optical constants do not depend on layer thickness, i.e. layer thickness dependence is captured fully by κ,

To evaluate if the model presented in Eq. (5) can accurately describe the experimental results, the function is fitted to the contrast data points for the samples with a 10 nm catalyst layer, for both λ = 500 and 1000 nm, and for three distinct hydrogen concentration steps. The results are presented in Fig. 12(a) and (b) with the fitted parameters given in Table 1.

The presented model can accurately describe the qualitative evolution of the contrast with different layer thicknesses. Furthermore, the change of the values upon hydrogen absorption seem reasonable; the intrinsic reflectance of the unloaded sensing layer for λ = 500 nm has even exactly the same value when we measured the reflectance of a 100 nm thick unloaded $Ta_{0.88}Pd_{0.12}$ sensing layer ($R_{sens,d=100nm} \approx$ 0.52). In addition, when applying this model to other capping layer thicknesses (5/30 nm) we get a reasonable qualitative description as well (Fig. 13).

Based on the model, we can derive four important conclusions. First of all, both the absorption and amplification coefficients for λ = 1000 nm are significantly lower compared to that of green light, and thus the light is less attenuated for IR light within the sensing layer than for green light. This is consistent with the values that we found for the unloaded samples (Fig. 10/Table S1) and also explains why the optical contrast of IR light continues to increase when the sensing layer

Table 1
Fitted parameters of the optical contrast from $Ta_{0.88}Pd_{0.12}$ sensing layers with 10 nm catalyst layer to the model as presented in Eq. (5).

C_{H_2}	λ = 500 nm						λ = 1000 nm					
	R_{sub}	R^*_{sens}	R^*_{cap}	κ_{sens}	κ_{cap}	α_{sens}	R_{sub}	R^*_{sens}	R^*_{cap}	κ_{sens}	κ_{cap}	α_{sens}
Unloaded	0.203	0.523	0.700	0.136	0.088	0.032	0.208	0.558	0.768	0.0403	0.085	0.013
0.016%	0.203	0.552	0.700	0.179	0.088	0.059	0.208	0.457	0.768	0.051	0.085	0.025
0.2%	0.203	0.557	0.700	0.191	0.088	0.070	0.208	0.445	0.768	0.051	0.085	0.026
4%	0.203	0.562	0.700	0.202	0.088	0.081	0.208	0.434	0.768	0.052	0.085	0.029

increases to $d_{sens} > 40$ nm.

In addition, the larger attenuation coefficient for green light in the sensing layer explains why the capping layer thickness has for larger thicknesses of the sensing layer hardly an influence on the optical contrast. For reasonably thick layers ($d_{sens} \gtrsim 40$ nm) the green light is simply already attenuated in the sensing layer before it can reach the capping layer. Hence, this light is not reflected. The capping layer has no influence on the optical contrast, it is solely determined by the change of the reflection coefficient of the substrate/$Ta_{0.88}Pd_{0.12}$ interface. Owing to the lower attenuation coefficient of IR light, the capping layer thickness continues to substantially influence the optical contrast at $\lambda = 1000$ nm for $d_{sens} \lesssim 80$ nm.

Furthermore, we observe that the non-monotonic dependence of the optical contrast with sensing layer thickness for $\lambda = 500$ nm is the result of three competing effects with different responses to hydrogen. For a small thickness of the sensing layer, the changing transmission with increasing C_{H2} has a negative effect on $\frac{R}{R_0}$ as can be inferred from the increase of α_{sens} with increasing C_{H2}. Differently, the sensing layer becomes more reflective: both as a result of an increase of R^*_{sens} and as a result of an increased value of κ_{sens}. These effects counter each other and explain why thicker capping layers in combination with $d_{sens} = 10$ nm result in a smaller contrast, as light attenuation within the sensing layer plays a more important role. In other words, when using a thin sensing layer, a significant portion of the light is reflected back for thicker catalyst layers which (negatively) 'contributes' to the signal.

Moreover, as both R^*_{sens} and κ_{sens} change considerably upon hydrogen absorption, thin sensing layers can, in combination with thin capping layers, result in a relatively large optical contrast. Indeed, for thin layers, the reflection increases both as a result of an increase of R^*_{sens} and an increase of κ_{sens}, while for much thicker sensing layers the latter contribution is negligible. This is in fact very advantageous, as it allows the construction of a very thin sensing stack with fast responses as only small quantities of hydrogen need to be dissociated at the surface of the catalyst.

Conductors reflect light well because the free electrons in the metal surface can interact with the incoming light [49]. Therefore, the increase of κ with increasing hydrogen content in the sensing layer may be explained due to the increase in free electron density in the system upon hydrogen absorption. It is known that when a metal hydride is formed, the H atom may donate an electron to the valence band, increasing the effective free electron density in the material. For example, in the solid solution α-Pd hydride, one hydrogen atom effectively contributes 0.75 free electrons to the valence band [50,51]. In $Ta_{0.88}Pd_{0.12}H_x$ such an effect may also occur. Increasing the conductivity of the material and limiting the penetration of light into the material as it has more chance to interact with the free electrons in the metal hydride, resulting in an increase in κ. In future studies, it would be interesting to perform an in-situ conductivity study of the sensing layer as it absorbs hydrogen to further reinforce this hypothesis. The findings can be related to models such as the Hagen-Rubens equation that relates the reflection of light in the infrared spectrum to the conductivity of a material [51].

3.4. Optical fibers

The next step is to deposit the layers on an optical fiber to realize the micro-mirror sensor of Fig. 1. For this, we have selected the configuration with a 20 nm $Ta_{0.88}Pd_{0.12}$ and 5 nm $Pd_{0.60}Au_{0.40}$ capping layer as this configuration provides the largest optical contrast for visible light.

To produce the micro-mirror sensor, we have stripped, cleaned and cleaved the optical fiber to obtain a flat and clean tip of the fiber. On this tip, we deposited the layers using magnetron sputtering (See experimental section for more details). Next, we evaluated the quality of the deposition using SEM and XRD measurements. The SEM images of Fig. S10 reveal that the fiber tip is indeed coated completely with a metallic coating. On the other hand, XRD measurements do not show any indication of the ⟨110⟩ reflection of body centered cubic α-Ta. This could be due because the material is not (i) textured, (ii) it is amorphous, or (iii) it has the β-Ta tetragonal structure [43]. A fourth possibility is that the signal from the tiny surface and thin layer is simply too small to be detected. To obtain the desired (textured) α-Ta phase we found that the thickness of the Ti adhesion layer on the fiber should be increased from 4 to 10 nm.

Subsequently, we tested the performance of the fiber as a hydrogen sensor. As illustrated in Fig. 1, the optical fiber on which the coating is deposited is connected to a beam splitter. On one end of the splitter light is coupled into the fiber, while on the side the light that was reflected by the metal hydride coating is transported towards the spectrometer. Fig. 14 presents the optical measurements of the micro-mirror sensor made out of the optical fiber with a 10 nm Ti adhesion layer, 20 nm $Ta_{0.88}Pd_{0.12}$ and 5 nm $Pd_{0.60}Au_{0.40}$ capping layer as a function of time for red light with $\lambda = 700$ nm. During this time, several steps in hydrogen pressure were made, first increasing the partial hydrogen pressure and subsequently decreasing the pressure. These steps are clearly reflected in the reflectivity of the optical fiber, showing well-defined and stable steps in the reflectivity. Furthermore, we see that the steps are completely free of hysteresis.

Next, we summarize the optical response of the fiber for multiple wavelengths across a wide range of partial hydrogen pressures/concentrations in the PRI diagram of Fig. 15(a). As a comparison, the figure also includes reflectivity measurements on substrate with the same sensing and capping layer and with a 4 (Fig. 15b) and 10 nm Ti adhesion layer (Fig. 15c).

We can deduce four main conclusions from Fig. 15. First of all, we see that the micro-mirror fiber sensor provides a monotonous response for wavelengths of $500 \leq \lambda \leq 750$ nm, thus including green and red light. This provides, together with the hysteresis-free nature of the sensor a direct relation between the optical response and the hydrogen concentration. For these wavelengths, we thus demonstrate a sensing range of 0.001% (10 ppm) $\leq C_{H2} \leq$ 100% in an inert gas environment. The lower limit here was merely limited by the set-up used, and the limit-of-detection of the sensor is likely to be much lower than 10 ppm based on earlier studies of the sensing material [4]. Given that the sensing material is the same as in Ref. [4], we expect that sub-second response times are possible with the sensor. We did not test this explicitly as the set-up was not optimized for such measurements and would merely reflect the response time of the set-up.

Second, we observe that the response of the fiber is qualitatively similar to that of the substrate with the same coating. Indeed, we observe the monotonous response for the visible light range, while a strong non-monotonous response is observed for IR light with a wavelength of 950 and 1000 nm. This is an important result, as it implies that the measurements on the substrates are representative for the result on the optical fibers.

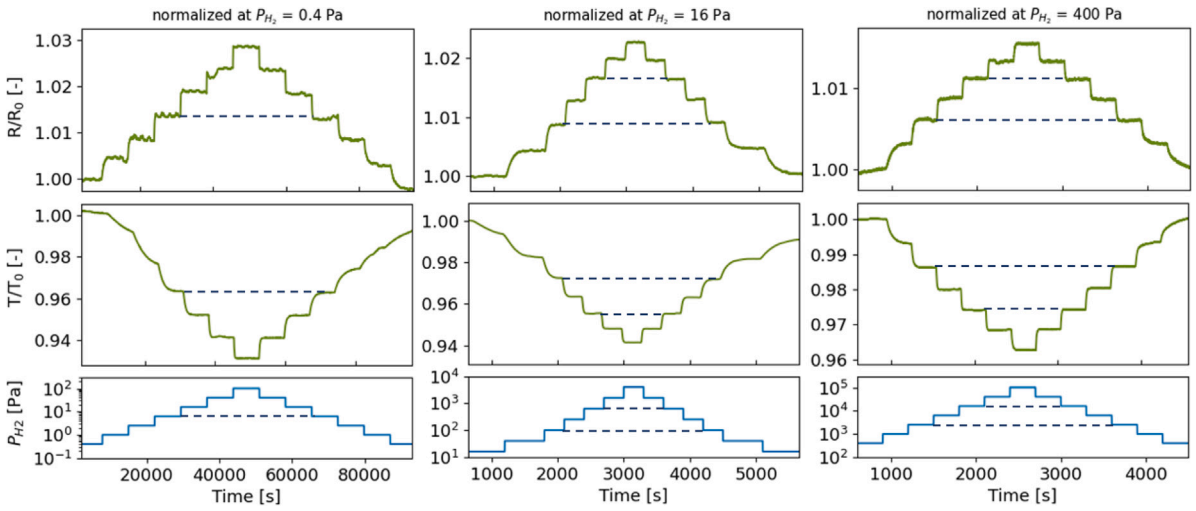

Fig. 14. Changes of the reflected intensity of λ = 700 nm light (binsize = 50 nm) of an optical fiber with a 10 nm Ti - 20 nm $Ta_{0.88}Pd_{0.12}$ - 5 nm $Pd_{0.60}Au_{0.40}$ coated on its tip as a function of time during which the partial hydrogen concentration/pressure was varied stepwise as indicated in the figure for the pressure range of (a) P_{H2} = 1.6 10^1 to 4 10^3 Pa and (b) P_{H2} = 4 ·10^2 to 10^5 Pa. The reflected intensity is normalized at the reflection of the lowest pressure point. The environment of the samples was at constant room temperature and atmospheric pressure. The dotted lines serve as guides to the eyes and indicate the same level of optical reflectivity/partial hydrogen pressure.

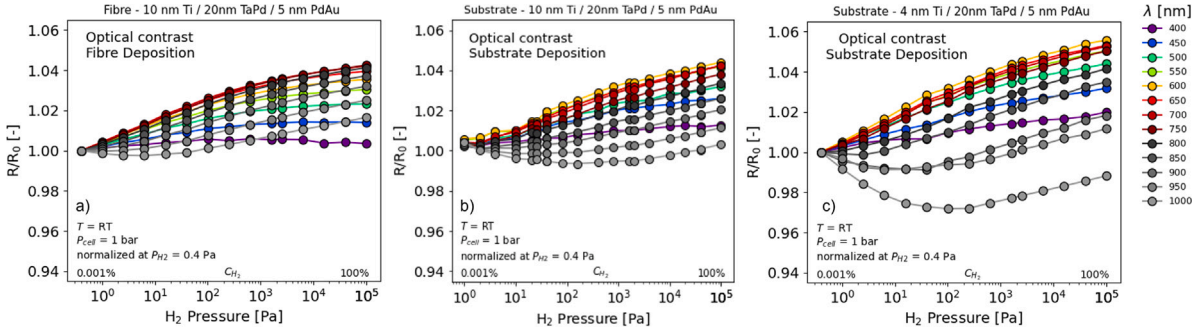

Fig. 15. PRI diagrams of the optical contrast in reflection for two sensing stack configurations at partial hydrogen pressures ranging from 0.4 Pa to 10^5 Pa measured at 1 bar at room temperature, binned per 50 nm with regard to wavelength of the signal for (a) a micro-mirror fiber with a 10 nm Ti - 20 nm $Ta_{0.88}Pd_{0.12}$ - 5 nm $Pd_{0.60}Au_{0.40}$ sensing stack deposited on the tip of the optical fiber, (b) 10 nm Ti - 20 nm $Ta_{0.88}Pd_{0.12}$ - 5 nm $Pd_{0.60}Au_{0.40}$ deposited on a substrate and (c) 4 nm Ti - 20 nm $Ta_{0.88}Pd_{0.12}$ - 5 nm $Pd_{0.60}Au_{0.40}$ deposited on a substrate.

Third, we estimate the resolution of the sensor. Figure S8 depicts the optical contrast of one particular hydrogen pressure step. It shows an intensity change of 1.0033 upon a hydrogen pressure step from 100 Pa to 256 Pa. To acquire the sensitivity across a larger range of hydrogen pressures, we fit the data points of the PRI diagram of Fig. 15(a) up until P_{H2} = 1.5 10^3, where the slope begins to drop slightly. This results in a slope of 0.0043 that is relatively constant with hydrogen pressure. The standard deviation of the signal is $\sigma \approx 0.000042$, which results in a relative accuracy for which we can detect a hydrogen pressure of $\Delta P_{H2}/P_{H2} = \Delta C_{H2}/C_{H2} \approx 0.010$.

Fourth, by comparing the measurements of a 4 (Fig. 15b) and 10 nm Ti adhesion layer (Fig. 15c) we find that the thicker adhesion layer results in a reduced optical contrast. We attribute this to the fact that the thicker Ti adhesion layer results in a larger reflectivity of the layer. As this reflectivity is largely unaffected by partial hydrogen pressure, this overall results in a reduced optical contrast according to Eq. (5). As such, to further improve the sensor one could investigate ways to reduce the reflectivity of the fiber(substrate)/adhesion layer interface. The model described in Section 3.3 shows that the potential is large: when this reflection is completely eliminated it could increase the sensitivity of the optical fiber by a factor 3 (Figure S9).

4. Conclusion

In conclusion, we have rationally developed a micro-mirror hydrogen sensor based on a tantalum-alloy as sensing layer. First, we studied the layer thickness dependence of the optical transmission and reflectivity of $Pd_{0.6}Au_{0.4}$ capped $Ta_{0.88}Pd_{0.12}$ thin films deposited on substrates. Modeling this result revealed that the reflected light signal is a complex interplay of attenuation, reflection and amplification coefficients of the $Ta_{0.88}Pd_{0.12}$ sensing and $Pd_{0.6}Au_{0.4}$ capping layer. These coefficients all depend on wavelength and hydrogen concentration/pressure, which adds to the complexity but also provides ample design opportunities. We selected the optimal thicknesses of the layers and fabricated an optical fiber sensor and demonstrate its performance both for visible and near infrared light. This sensor provides hysteresis-free hydrogen sensing across at least five orders of magnitude in hydrogen concentration.

CRediT authorship contribution statement

D.J. Verhoeff: Writing – review & editing, Writing – original draft, Visualization, Validation, Software, Methodology, Investigation, Formal analysis, Data curation, Conceptualization. **H. Schreuders:** Writing – review & editing, Validation, Supervision, Software, Methodology, Investigation, Data curation. **L.J. Bannenberg:** Writing – review & editing, Writing – original draft, Visualization, Validation, Supervision, Software, Resources, Project administration, Methodology, Investigation, Funding acquisition, Formal analysis, Data curation, Conceptualization.

Declaration of competing interest

The authors declare the following financial interests/personal relationships which may be considered as potential competing interests: Lars J. Bannenberg and Herman Schreuders reports financial support was provided by the European Union through the Horizon Europe Grant 'OVERLEAF' (Grant number 101056818) and through the Clean aviation grant 'HYDEA' (Grant number 101102019). Lars Bannenberg and Herman Schreuders have patent # WO 2022/098230 issued to Delft University of Technology. If there are other authors, they declare that they have no known competing financial interests or personal relationships that could have appeared to influence the work reported in this paper.

Acknowledgments

We are grateful for financial support from the European Union through the Horizon Europe Grant 'OVERLEAF' (Grant number 101056818) and through the Clean aviation grant 'HYDEA' (Grant number 101102019). Roger Groves, Sandra Dewi and Kasun Dissanayake are thanked for fruitful discussions. Bart Boshuizen is greatly thanked for designing and maintaining Labview software to control the pressure cells. Erwin Janssen and Jörg Haberlah are thanked for providing the gas cylinders. This manuscript is based on the MSc thesis in Applied Physics entitled 'Towards a Practical Hydrogen Sensor; Optical Response Analysis on new Geometries for $Ta_{0.88}Pd_{0.12}$ based Metal-Hydride Hydrogen Sensors, and Characterization of Structure at Low Temperatures' successfully defended by Daan J. Verhoeff at Delft University of Technology.

Appendix A. Supplementary data

Exemplary XRD data, Exemplary XRR data, Response time data, Optical contrast in transmission. XRD data on optical fiber. Illustration of resolution. Modeled optical contrast with various reflections of the substrate.

Supplementary material related to this article can be found online at https://doi.org/10.1016/j.snb.2025.137229.

Data availability

Data will be made available on request.

References

[1] T. Hübert, L. Boon-Brett, G. Black, U. Banach, Hydrogen sensors–a review, Sensors Actuators B 157 (2) (2011) 329–352.
[2] W.J. Buttner, M.B. Post, R. Burgess, C. Rivkin, An overview of hydrogen safety sensors and requirements, Int. J. Hydrog. Energy 36 (3) (2011) 2462–2470.
[3] F.A.A. Nugroho, I. Darmadi, L. Cusinato, A. Susarrey-Arce, H. Schreuders, L.J. Bannenberg, A. Bastos da Silva Fanta, S. Kadkhodazadeh, J.B. Wagner, T.J. Antosiewicz, A. Hellman, V.P. Zhdanov, B. Dam, C. Langhammer, Metal-polymer hybrid nanomaterials for plasmonic ultrafast hydrogen detection, Nature Mater. 18 (2019) 489–495.
[4] L.J. Bannenberg, H. Schreuders, B. Dam, Tantalum-palladium: Hysteresis-free optical hydrogen sensor over 7 orders of magnitude in pressure with sub-second response, Adv. Funct. Mater. 31 (2021) 2010483.
[5] F.A.A. Nugroho, P. Bai, I. Darmadi, G.W. Castellanos, J. Fritzsche, C. Langhammer, J. Gómez Rivas, A. Baldi, Inverse designed plasmonic metasurface with parts per billion optical hydrogen detection, Nature Commun. 13 (1) (2022) 5737.
[6] C. Wadell, S. Syrenova, C. Langhammer, Plasmonic hydrogen sensing with nanostructured metal hydrides, ACS Nano 8 (12) (2014) 11925–11940.
[7] L.J. Bannenberg, C. Boelsma, K. Asano, H. Schreuders, B. Dam, Metal hydride based optical hydrogen sensors, J. Phys. Soc. Japan 89 (5) (2020) 051003.
[8] L.J. Bannenberg, M. Heere, H. Benzidi, J. Montero, E. Dematteis, S. Suwarno, T. Jaroń, M. Winny, P. Orłowski, W. Wegner, A. Starobrat, K. Fijałkowski, W. Grochala, Z. Qian, J.-P. Bonnet, I. Nuta, W. Lohstroh, C. Zlotea, O. Mounkachi, F. Cuevas, C. Chatillon, M. Latroche, M. Fichtner, M. Baricco, B. Hauback, A. El Kharbachi, Metal (boro-) hydrides for high energy density storage and relevant emerging technologies, Int. J. Hydrog. Energy 45 (58) (2020) 33687–33730.
[9] I. Darmadi, F.A.A. Nugroho, C. Langhammer, High-performance nanostructured palladium-based hydrogen sensors–current limitations and strategies for their mitigation, ACS Sens. 5 (11) (2020) 3306–3327.
[10] W.-T. Koo, H.-J. Cho, D.-H. Kim, Y.H. Kim, H. Shin, R.M. Penner, I.-D. Kim, Chemiresistive hydrogen sensors: Fundamentals, recent advances, and challenges, ACS Nano 14 (11) (2020) 14284–14322.
[11] K. Chen, D. Yuan, Y. Zhao, Review of optical hydrogen sensors based on metal hydrides: Recent developments and challenges, Opt. Laser Technol. 137 (2021) 106808.
[12] Y.-n. Zhang, H. Peng, X. Qian, Y. Zhang, G. An, Y. Zhao, Recent advancements in optical fiber hydrogen sensors, Sensors Actuators B 244 (2017) 393–416.
[13] G. Wang, J. Dai, M. Yang, Fiber-optic hydrogen sensors: A review, IEEE Sens. J. 21 (11) (2020) 12706–12718.
[14] N.P. Brandon, Z. Kurban, Clean energy and the hydrogen economy, Phil. Trans. R. Soc. A 375 (2098) (2017) 20160400.
[15] Editorial, Hydrogen to the rescue, Nature Mater. 17 (565) (2020).
[16] J.O. Abe, A.P.I. Popoola, E. Ajenifuja, O.M. Popoola, Hydrogen energy, economy and storage: Review and recommendation, Int. J. Hydrog. Energy 44 (29) (2019) 15072–15086.
[17] G. Glenk, S. Reichelstein, Economics of converting renewable power to hydrogen, Nat. Energy 4 (3) (2019) 216–222.
[18] A. Bakenne, W. Nuttall, N. Kazantzis, Sankey-diagram-based insights into the hydrogen economy of today, Int. J. Hydrog. Energy 41 (19) (2016) 7744–7753.
[19] A. El Kharbachi, E.M. Dematteis, K. Shinzato, S.C. Stevenson, L.J. Bannenberg, M. Heere, C. Zlotea, P.A. Szilágyi, J.-P. Bonnet, W. Grochala, et al., Metal hydrides and related materials. Energy carriers for novel hydrogen and electrochemical storage, J. Phys. Chem. C 124 (14) (2020) 7599–7607.
[20] N. Warwick, P. Griffiths, J. Keeble, A. Archibald, J. Pyle, K. Shine, Atmospheric implications of increased Hydrogen use, 2022, AvaliableAt: https://assets.publishing.service.gov.uk/government/uploads/system/uploads/attachment_data/file/1067144/atmospheric-implications-of-increased-hydrogen-use.pdf. 75.
[21] M.A. Butler, Fiber optic sensor for hydrogen concentrations near the explosive limit, J. Electrochem. Soc. 138 (9) (1991) L46–L47.
[22] M.A. Butler, Micromirror optical-fiber hydrogen sensor, Sensors Actuators B 22 (2) (1994) 155–163.
[23] E. Herkert, F. Sterl, N. Strohfeldt, R. Walter, H. Giessen, Low-cost hydrogen sensor in the ppm range with purely optical readout, ACS Sens. 5 (4) (2020) 978–983.
[24] Z. Zhao, M.A. Carpenter, H. Xia, D. Welch, All-optical hydrogen sensor based on a high alloy content palladium thin film, Sensors Actuators B 113 (1) (2006) 532–538.
[25] R.J. Westerwaal, J.S.A. Rooijmans, L. Leclercq, D.G. Gheorghe, T. Radeva, L. Mooij, T. Mak, L. Polak, M. Slaman, B. Dam, T. Rasing, Nanostructured Pd-Au based fiber optic sensors for probing hydrogen concentrations in gas mixtures, Int. J. Hydrog. Energy 38 (10) (2013) 4201–4212.
[26] C. Wadell, F.A.A. Nugroho, E. Lidstrom, B. Iandolo, J.B. Wagner, C. Langhammer, Hysteresis-free nanoplasmonic Pd–Au alloy hydrogen sensors, Nano Lett. 15 (5) (2015) 3563–3570.
[27] F.A.A. Nugroho, I. Darmadi, V.P. Zhdanov, C. Langhammer, Universal scaling and design rules of hydrogen induced optical properties in Pd and Pd-alloy nanoparticles, ACS Nano 12 (10) (2018) 9903–9912.
[28] I. Darmadi, F.A.A. Nugroho, S. Kadkhodazadeh, J.B. Wagner, C. Langhammer, Rationally designed PdAuCu ternary alloy nanoparticles for intrinsically deactivation-resistant ultrafast plasmonic hydrogen sensing, ACS Sens. 4 (5) (2019) 1424–1432.
[29] L.J. Bannenberg, F.A.A. Nugroho, H. Schreuders, B. Norder, T.T. Trinh, N.-J. Steinke, A.A. Van Well, C. Langhammer, B. Dam, Direct comparison of PdAu alloy thin films and nanoparticles upon hydrogen exposure, ACS Appl. Mater. Interfaces 11 (17) (2019) 15489–15497.
[30] K.J. Palm, J.B. Murray, J.P. McClure, M.S. Leite, J.N. Munday, In situ optical and stress characterization of alloyed Pd_xAu_{1-x} hydrides, ACS Appl. Mater. Interfaces 11 (48) (2019) 45057–45067.
[31] H.M. Luong, M.T. Pham, T. Guin, R.P. Madhogaria, M.-H. Phan, G.K. Larsen, T.D. Nguyen, Sub-second and ppm-level optical sensing of hydrogen using templated control of nano-hydride geometry and composition, Nat. Commun. 12 (1) (2021) 2414.
[32] C. Zhang, C. Shen, X. Liu, S. Liu, H. Chen, Z. Huang, Z. Wang, T. Lang, C. Zhao, Y. Zhang, Pd/Au nanofilms based tilted fiber Bragg grating hydrogen sensor, Opt. Commun. 502 (2022) 127424.
[33] D. Tomeček, H.K. Moberg, S. Nilsson, A. Theodoridis, I. Darmadi, D. Midtvedt, G. Volpe, O. Andersson, C. Langhammer, Neural network enabled nanoplasmonic hydrogen sensors with 100 ppm limit of detection in humid air, Nature Commun. 15 (1) (2024) 1208.
[34] C. Boelsma, L.J. Bannenberg, M.J. van Setten, N.-J. Steinke, A.A. Van Well, B. Dam, Hafnium - an optical hydrogen sensor spanning six orders in pressure, Nature Commun. 8 (2017) 15718.
[35] L.J. Bannenberg, C. Boelsma, H. Schreuders, S. Francke, N.-J. Steinke, A.A. Van Well, B. Dam, Optical hydrogen sensing beyond palladium: Hafnium and tantalum as effective sensing materials, Sensors Actuators B 283 (2019) 538–548.

[36] L.J. Bannenberg, H. Schreuders, H. Kim, K. Sakaki, S. Hayashi, K. Ikeda, T. Otomo, K. Asano, B. Dam, Suppression of the phase coexistence of the fcc–fct transition in hafnium-hydride thin films, J. Phys. Chem. Lett. 12 (45) (2021) 10969–10974.
[37] L.J. Bannenberg, L. Blom, K. Sakaki, K. Asano, H. Schreuders, Completely elastic deformation of hydrogenated Ta thin films, ACS Mater. Lett. 5 (2023) 962–969.
[38] L.J. Bannenberg, H. Schreuders, N. van Beugen, C. Kinane, S. Hall, B. Dam, Tuning the properties of thin film TaRu for hydrogen sensing applications, ACS Appl. Mater. Interfaces 15 (6) (2023) 8033–8045.
[39] L.J. Bannenberg, B. Boshuizen, F.A. Ardy Nugroho, H. Schreuders, Hydrogenation kinetics of metal hydride catalytic layers, ACS Appl. Mater. Interfaces 13 (44) (2021) 52530–52541.
[40] W. Hu, B. Xue, J. Dai, K. Yin, Z. Chen, M. Yang, Quasi-distributed optical fiber hydrogen leakage detecting system based on bus chain topology structure, Opt. Express 32 (11) (2024) 19242–19251.
[41] P. Ngene, R.J. Westerwaal, S. Sachdeva, W. Haije, L.C. de Smet, B. Dam, Polymer-induced surface modifications of Pd-based thin films leading to improved kinetics in hydrogen sensing and energy storage applications, Angew. Chem. Int. Ed. 53 (45) (2014) 12081–12085.
[42] R. Delmelle, P. Ngene, B. Dam, D. Bleiner, A. Borgschulte, Promotion of hydrogen desorption from palladium surfaces by fluoropolymer coating, ChemCatChem 8 (9) (2016) 1646–1650.
[43] L.J. Bannenberg, D.J. Verhoeff, N. Jonckers Newton, M. Thijs, H. Schreuders, Structural and optical properties of thin film β-Ta upon exposure to hydrogen to asses its applicability as hydrogen sensing material, ACS Appl. Nano Mater. 7 (2) (2024) 1757–1766.
[44] T. Shiraishi, R.J.D. Tilley, An estimation of the reflectivity of gold-and platinum-group metals alloyed with copper, J. Mater. Sci. 49 (2014) 3461–3468.
[45] M. Björck, G. Andersson, GenX: an extensible X-ray reflectivity refinement program utilizing differential evolution, J. Appl. Crystallogr. 40 (6) (2007) 1174–1178.
[46] A. Glavic, M. Björck, GenX 3: the latest generation of an established tool, J. Appl. Crystallogr. 55 (4) (2022) 1063–1071.
[47] X. Sun, R. Hong, H. Hou, Z. Fan, J. Shao, Thickness dependence of structure and optical properties of silver films deposited by magnetron sputtering, Thin Solid Films 515 (17) (2007) 6962–6966.
[48] L.J. Bannenberg, Algorithm to suppress drift for micro-mirror and other intensity modulated hydrogen sensors, IEEE Sens. J. 23 (24) (2023) 30720–30727.
[49] W.D. Callister Jr., D.G. Rethwisch, Callister's Materials Science and Engineering, John Wiley & Sons, 2020.
[50] E. Del Giudice, A. De Ninno, M. Fleischmann, A. Frattolillo, G. Mengoli, Loading of H (D) in a Pd lattice, in: The 9th International Conference on Cold Fusion, Condensed Matter Nuclear Science, 2002.
[51] R.E. Hummel, R.E. Hummel, Atomistic theory of the optical properties, in: Electronic Properties of Materials, Springer, 2011, pp. 227–246.

Daan Verhoeff graduated from as an master of science in applied physics from Delft University of Technology in 2023. Within the study program, he followed the Energy and Instrumentation tracks. As his master thesis, he developed and optimized a practical hydrogen gas sensor. Part of his master thesis forms the foundation of this manuscript. After graduation, Daan joined TNO, a research and development institute for applied research. Here, he joined a trainee-ship program and is currently involved in developing the value proposition of high tech manufacturing opportunities for hydrogen electrolysers.

Herman Schreuders obtained his bachelor in engineering physics from the Hogeschool Rijswijk, the Netherlands. Subsequently, he moved to Eindhoven where he joined Philips Research. There, he researched cathode ray tubes, liquid crystal displays and plasma displays. In 2003, Herman started as an engineer in the Condensed Matter Physics Group of the Vrije Universiteit in Amsterdam and in 2009 he joined Delft University of Technology. His main responsibilities are to perform depositions of thin films by magnetron sputtering and design and maintain novel experimental apparatus. He actively contributes to research on hydrogen sensors, switchable mirrors and lightweight hydrogen storage materials.

Lars Bannenberg is an assistant professor at Delft University of Technology, The Netherlands. Lars received his MSc in financial economics from Erasmus University Rotterdam in 2015, as well as MSc (2015) and PhD degrees (2019) in applied physics from Delft University of Technology. His research interests include thin film materials and interfaces of energy materials such as batteries and materials for optical hydrogen sensors. To study these materials, Lars uses a wide range of neutron- and x-ray scattering techniques. At present, he is also responsible for the neutron reflectometer at the TU Delft Reactor Institute.